Paik *et al. Micro & Nano Manufacturing* (2025) 1:1
https://doi.org/10.1007/s44374-024-00001-2

Micro & Nano Manufacturing

RESEARCH Open Access

Iridescent structural color by using ultra-low refractive index aerogel as optical cavity dielectric

Jennie Paik[1], Wei-Jie Feng[1], Sean W. Clark[2], Hyeonwoo Kim[3] and L. Jay Guo[1,3*]

Abstract

Iridescent color-shift pigments have been used in some industrial applications, e.g., for cosmetics and packaging. To achieve environmental-friendly and lasting color, thin-film interference is used to generate structural color. By maximizing the refractive index (RI) difference between the thin films (i.e., using an ultralow RI film), super-iridescent structural color can be produced. While the lowest refractive index of a naturally occurring solid dielectric is close to 1.37 (i.e., MgF_2), we synthesized highly porous dielectric SiO_2 aerogel to achieve ultralow-RI ($n \sim 1.06$) and demonstrated a high-refractive index/low-refractive index/absorber (HLA) trilayer structural color. The achieved structural color is highly iridescent and capable of tracing a near-closed loop in CIE color space. By tuning the refractive index, thickness, and geometry of the aerogel layer, we control the reflection dip's shape, therefore producing a wide range of vivid and iridescent colors.

Keywords Structural color, Aerogel, Fabry–perot cavity, Iridescence, Sol–gel, Solution process

Introduction

Iridescence, or changes in color with angle of observation, is an attractive optical phenomenon commonly found in nature. Insight into the microstructure of insect wings, bird feathers, and seashells shows that iridescence is enabled by thin-film interference, a type of structural color: the interaction of light with layers of different refractive indices on a sufficiently small scale [1, 2]. This is impossible to achieve through chemical dye- or fluorophore-based methods, both naturally and synthetically. Thus, developing iridescent structural colors based on thin-film interference is of contemporary interest in materials science and engineering.

Structural colors are advantageous because they are photo- and chemostable, more environmentally conscious, and can achieve a wide range of hue, saturation, and brightness with a very small chemical library [3]. Though angle-tolerant color is often required for consistent color perception in decoration, angle-variable color is desirable for certain applications (e.g., luxury packaging, certain types of automotive pigments, anti-counterfeiting, colorimetric sensing) to give a distinct, color-shifting appearance. To address this, we developed a high-refractive index/low-refractive index/absorber (HLA) tri-layer structural color using SiO_2 aerogel as the low-RI dielectric. Due to its high porosity, SiO_2 aerogel has many unique properties including ultra-low density (~ 1 mg cm^{-3}), ultra-low refractive index, very high surface area, and very low thermal conductivity. This enables aerogel usage in a wide range of potential applications including energy storage, optical coating, catalysis, and thermal insulation [4–27]. Even so, the incorporation of

*Correspondence:
L. Jay Guo
guo@umich.edu
[1] Macromolecular Science and Engineering, University of Michigan, Ann Arbor, MI 48109, USA
[2] Department of Chemical Engineering, University of Florida, Gainesville, FL 32611, USA
[3] Department of Electrical Engineering and Computer Science, University of Michigan, Ann Arbor, MI 48109, USA

aerogel into a cavity structure as a dielectric spacer for structural color applications has hardly been studied. Herein, for the first time, SiO_2 aerogel has been introduced as an ultra-low refractive index dielectric within a $TiO_2/SiO_2/Si$ system asymmetric F-P cavity, and its color performance is investigated. The ultra-low refractive index of aerogel is close to that of air ($n \sim 1.06$). Thus, the color can travel a large arc on the CIE diagram upon angle variation.

Structural colors from thin-film interference can be understood by considering the optical path length difference between a directly reflected beam and a beam undergoing multiple reflections within the film as shown in Fig. 1a (assuming air as the incident medium). The optical path length difference between the initial reflected beam and the beam reflected through the film dictates which light wavelengths will constructively or destructively interfere, thereby generating color through interference effect [28, 29]. The refractive index of the film plays a very important role in determining the overall angle sensitivity $\frac{\delta\lambda}{\delta\theta}$, as a wider angle can decrease the path length difference, thereby blue-shifting the resonant wavelength. As shown in Fig. 1b, a very large shift in resonance wavelength is observed with a low refractive

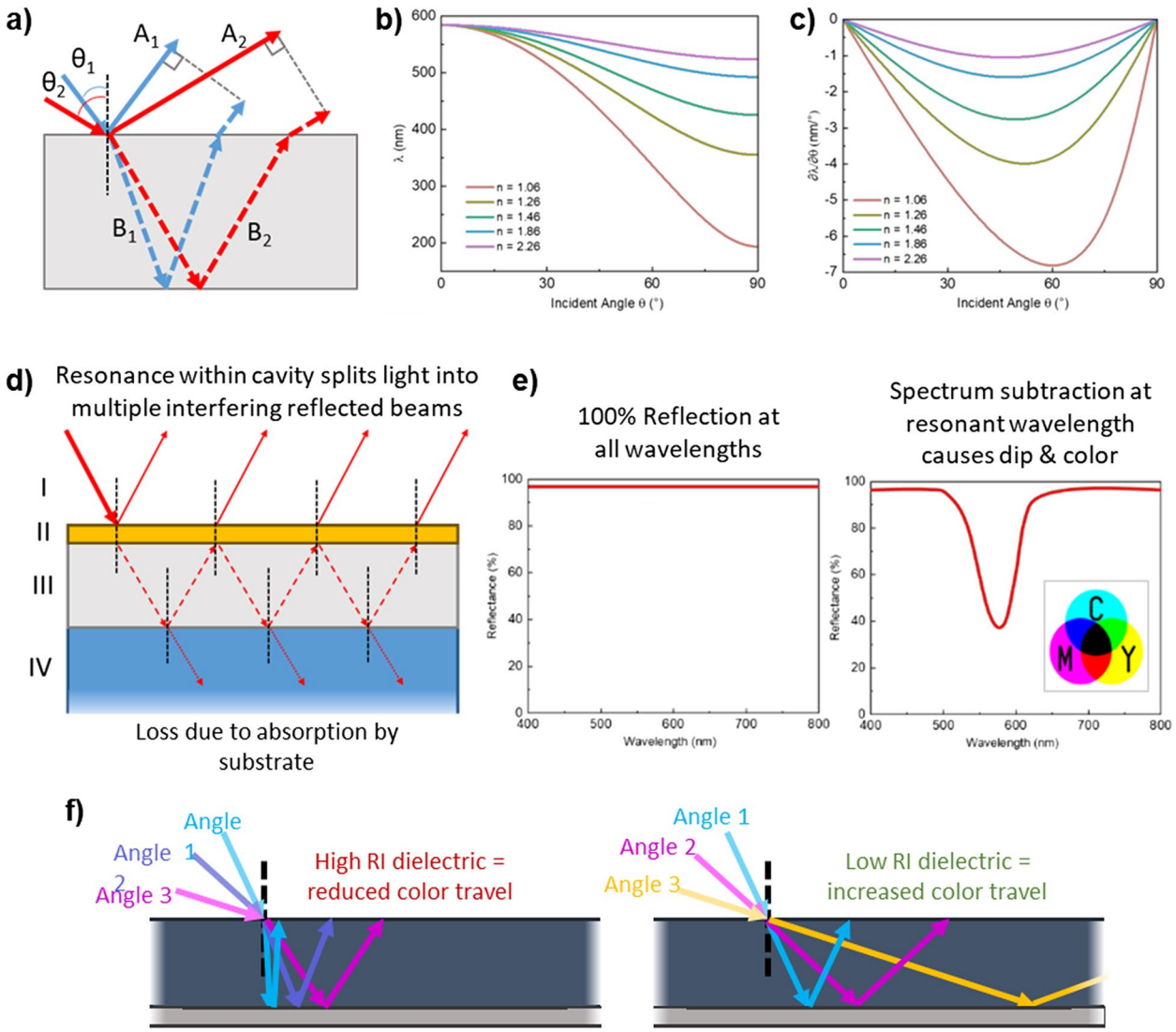

Fig. 1 **a** Schematic illustration of Bragg's law in a thin film. **b** Resonance wavelength shift with respect to incident angles based on Eq. 1 and **c** angle-dependent sensitivity based on Eq. 2 with refractive index varying from 1.06 to 2.26. **d** Schematic of cavity resonance in a high-low-absorber (HLA) structural color film. **e** Subtraction of resonant wavelength from perfect reflection results in CMY color. **f** Schematic of effect of refractive index on color travel

index, while the resonance wavelength hardly moves when the medium refractive index becomes high which is often exploited for angle-insensitive colors [30–32]. In addition, the color change becomes more rapid at larger angles for low refractive index medium (Fig. 1c).

To enhance color perception, we can incorporate the thin film into a cavity consisting of an optically thin high refractive index (RI) layer atop a lower RI dielectric and a partially absorbing and reflecting bottom layer (Fig. 1d). This high-low-absorber (HLA) structure is a generalization of an asymmetric Fabry–Perot (FP) cavity, thus similar principles apply [30]. The dielectric forms a cavity where incident waves partially reflect and partially transmit at the cavity boundaries formed by the top high index and bottom absorber layers (II–III and III–IV in Fig. 1d). The perceived color is controlled by varying the thickness of the resonator cavity. Multiple beam interference produces a resonance condition where light of a selected wavelength is strongly absorbed by the bottom absorber layer, leading to subtractive color (Fig. 1e). The low RI dielectric allows for a wide range of optical path length differences, resulting in highly angle-dependent colors. The purity of the subtractive color in the HLA structure depends on a balance of the absorption loss by the absorber material and the radiation loss of the cavity [30].

To allow for high optical path length variation, commercial iridescent color-shift pigments use TiO_2 (RI = 2.2) and SiO_2 (RI = 1.46) and other systems with a large refractive index difference [33]. However, the lowest refractive index of a naturally occurring solid dielectric is close to 1.37 (i.e., MgF_2), which is still not significantly lower than SiO_2 [34–36]. A potential new addition to the material library is a dielectric aerogel, whose ultralow refractive index arises from high structural porosity: the air volume occupancy is typically around 95–99% but could go even higher to 99.98% [34–38]. SiO_2 aerogel is synthesized through sol–gel chemistry via a hydrolysis-condensation reaction [39, 40]. Hydrolysis of an organosilane precursor (most often tetramethyl- or tetraethylorthosilicate (TMOS or TEOS)) is followed by condensation into SiO_2 nanoparticles, which further undergo agglomeration once the nanoparticles reach a critical size. As more SiO_2 nanoparticles join, a highly porous SiO_2 network is formed [39–41]. To produce the HLA structural color, we use titanium dioxide (TiO_2, RI ~ 1.8–2.4) or aluminum (Al, RI ~ 1.37 at 632.8 nm) as a top reflector, and Si substrate as the bottom absorber on which the aerogel layer is deposited. We achieved a highly iridescent structural color capable of tracing a near-closed loop in CIE color space. By tuning the refractive index, thickness, and geometry of the underlying structures, we control the reflection dip's travel, therefore producing a wide range of iridescent colors.

Experimental

Materials

Acetone (58.08 g/mol, ACS grade, Fisher Scientific, Hanover Park, IL), ethanol (46.068 g/mol, ACS grade, Fisher Scientific, Hanover Park, IL), hexanes (86.17 g/mol ACS grade, Fischer Scientific, Hanover Park, IL), toluene (92.14 g/mol, ACS grade, Fisher Scientific, Hanover Park, IL), chlorotrimethylsilane (TCMS, 108.64 g/mol, puriss > 99.0%, Sigma-Aldrich, St. Louis, MO), tetraethyl orthosilicate (TEOS, 208.33 g/mol, 98% ACS grade, Sigma-Aldrich, St. Louis, MO), 3-aminopropyl triethoxysilane (APTES, 221.372 g/mol, Sigma-Aldrich, St. Louis, MO), gold(III) chloride trihydrate ($HAuCl_4{}^*3H_2O$, 339.79 g/mol anhydrous basis, Sigma-Aldrich St. Louis, MO), sodium citrate dihydrate ($HOC(COONa)(CH_2COONa)_2{}^*2H_2O$, 294.10 g/mol, ACS reagent, Sigma-Aldrich, St. Louis, MO), nitrogen gas (N_2, industrial grade, Metro Welding, Detroit, MI) were used as received. Milli-Q water with a resistivity of > 18.2 MΩ was used throughout. p-Si(100) wafers of 400 μm thickness were diced and used as substrate.

Substrate preparation

Prior to coating, silicon wafers were cut into roughly $1'' \times 1''$ pieces and then sequentially sonicated in acetone, ethanol, and water for 5 min with drying under N_2 flow between each bath.

Aerogel synthesis and deposition

A hydrolysis-condensation sol–gel reaction was used to prepare SiO_2 aerogel of RI = 1.06 from TEOS. Into a base-cleaned and dry 100 mL glass media bottle, 11.1 mL ethanol (0.190 mol), 0.4 mL water (0.022 mol), and 11.1 mL TEOS (0.050 mol) were added in order under stirring. 0.5 mL 0.1 M hydrochloric acid (HCl) (0.0005 mol) was added slowly to adjust the pH to 3, resulting in a molar ratio of TEOS:EtOH:water:HCl = 1:3.8:1.1:0.001. The bottle was capped and left to stir at room temperature for 90 min to ensure full hydrolysis of TEOS. Condensation was initiated by adding another 102 mL of ethanol (1.749 mol) followed by 1.25 mL 28 wt% ammonium hydroxide (NH_4OH, 0.010 mol) to give a molar ratio of TEOS:EtOH:water:HCl:NH_4OH = 1:38.8:3.6:0.001:0.004. After mixing, the resulting sol was capped and aged for 7–10 days in a 55 °C oven to complete hydrolysis, condensation, and aging, after which a wet porous, translucent gel is formed. The molar ratio of TEOS can be changed to increase the refractive index of the aerogel, adjusting ethanol accordingly to keep the total volume consistent. Aerogel suspensions with RI of 1.14 and 1.23 were prepared by adding 1.5 (0.074 mol) and 2 times (0.099 mol) more TEOS, respectively. Full details of this synthesis are available in Table S1.

The wet gel was washed 3 times in ethanol at 55 °C at 1-h intervals to remove residual unreacted material, followed by a solvent exchange in hexane at 55 °C for 1 h. To resist network collapse during ambient pressure processing, hydrophobization of the wet gel was performed by submerging into 200 mL of 5 vol% TCMS in hexane (0.079 mol TCMS) for 24 h at 55 °C. Two additional hexane washes were performed at 55 °C at 1-h intervals to remove unreacted TMCS. The gel was then redispersed into 200 mL hexane and subjected to pulsed tip sonication (Cole-Parmer 500W Ultrasonic Homogenizer) in cycles of 59 s on, 16 s off totaling 1 h of pulse-on time. The gel was then vacuum filtered to remove large debris in the suspension. Drying over a molecular sieve can be performed to remove infiltrated water if necessary. The resulting aerogel suspension is mixed with an equal volume amount of toluene prior to spin-coating. Thickness control was achieved by diluting the aerogel stock suspension with 1:1 volume hexane:toluene solutions at different volume ratios.

The SiO_2 aerogel solution was drop-cast onto a substrate followed by spin coating (SETCAS LLC KW-4L Spin Coater) at 1000 rpm for 60 s with 500 rpm s^{-1} ramp-up. The as-coated sample was baked on a 100 °C hot plate. Various thicknesses were achieved by spin-coating multiple layers of stock and dilute aerogel solutions. After the desired thickness was achieved, films were baked at 150 °C for 30 min in a convection oven to release residual film stress.

Gold nanoparticle synthesis

Citrate anion-capped gold nanoparticles (AuNPs) were prepared by reduction from $HAuCl_4$ in aqueous media. Into a 250-mL double-necked round-bottomed-flask (double-necked RBF), 100 mL of 1 mM $HAuCl_4$ was added. The small neck was stoppered and a cold-water condenser was placed in the large neck. The solution was refluxed at 100 °C under vigorous stirring (~ 800 rpm) for 15 min. Into the small neck, 10 mL of 38.8 mM sodium citrate solution was quickly added. Over the next 3 min, the solution changed from pale yellow to dark bluish-gray to deep burgundy, indicating the growth of AuNPs. The solution was refluxed at 100 °C for another 15 min, then cooled to room temperature under continuous stirring, after which they were ready to use.

Functionalization of aerogel with gold nanoparticles

Functionalization of aerogel with gold nanoparticles was mediated by APTES. First, spin-coated aerogel films on Si wafers were baked in a furnace at 500 °C for 6 h to burn away TMCS and other residual nonpolar organics, after which the films were submerged in a solution of 10 wt% APTES in EtOH for 1 h. The pieces were removed and thoroughly rinsed with EtOH and Milli-Q water, then dried under N_2 flow. The aerogel films were then immersed in AuNP solution for 1 h to ensure adsorption of AuNPs to the aerogel, followed by rinsing with Milli-Q water to remove unadsorbed AuNPs.

HLA fabrication

To complete the HLA structure, Al or TiO_2 were deposited on the aerogel films by electron beam evaporation deposition (Evovac Evaporator, Angstrom Engineering). Initial TiO_2 deposition was performed at a rate of 5 Å/s to 5 nm thickness followed by deposition at 1 Å/s until desired thickness was reached. Al deposition was performed at 5 Å/s until desired thickness was reached.

HLA film characterization

Specular reflection spectra at normal incidence were measured using a thin-film measurement instrument integrated with a spectrometer (HR4000CG-UV-NIR, Ocean Insight) and a white halogen light source (HL-2000-FHSA, Ocean Insight). Angle-resolved specular reflection spectra were measured with a UV–Vis-NIR spectrometer (Lambda 1050, PerkinElmer Inc.) integrated with a Universal Reflectance Accessory. Diffuse reflectance (8°/day), specular + diffuse reflectance (8°/h), and transmission measurements were collected using the 150 mm InGaAs integrating sphere module (PerkinElmer, Inc.). Angle-resolved reflection spectra for s- and p-polarized light between 45 and 75° were collected on a spectroscopic ellipsometer (M-2000, J.A. Woollam Co. at angles between 45 and 75°; VASE®, J.A. Woollam Co. at angles between 20 and 45°). Imaging and elemental distribution were performed using TEM/EDS (Thermo Fisher Spectra 300 Probe-Corrected S/TEM). The surface morphology was investigated using FE-SEM (SU8000, Hitachi) at 2 kV accelerating voltage. Aerogel and TiO_2 refractive indices were measured using spectroscopic ellipsometry (M-2000, J.A. Woollam Co.) and fit using CompleteEase 6.7. HLA structure models were constructed in CompleteEase 6.7 using measured data.

Optical simulation

Simulated reflectance spectra and color appearance were calculated in MATLAB R2023b based on the transfer matrix method considering the aerogel as an effective medium [42]. Optical dispersion of each layer was extracted from spectroscopic ellipsometer data as inputs. An adjusted model was fitted using the Bruggeman Effective Medium Approximation method with a gradual change in volume fraction to account for mixing as a function of depth.

Results and discussion

Porosity and refractive index controlled by silica precursor concentration

Aerogel is a highly porous structure with most of the space filled with air. As described in detail in the method section above, aerogel synthesis from TEOS proceeds via hydrolysis-condensation [39, 40]. Under acidic conditions (pH ~ 3), TEOS is hydrolyzed into $Si(OH)_n(OEt)_{4-n}$ $(1 < n < 4)$ [41]. Condensation into SiO_2 networks is triggered by raising the pH to slightly basic conditions (pH ~ 8). First, SiO_2 particles are formed in solution and grow to a critical size, followed by assembly of these particles into a solvent-swollen SiO_2 network [41]. To remove solvent and form air voids without collapsing the delicate framework, fast extraction of the solvent is typically carried out with either critical point drying or freeze drying, thus yielding a bulk aerogel [6, 43]. However, it is neither practical nor feasible to coat a thin (submicrometer thick) aerogel film due to the lack of control over film thickness or uniformity. To enhance the rate of solvent removal during spin-coating and therefore enable processing at ambient conditions, aerogel particles are dispersed into a volatile solvent like hexane. However, using hexane alone will cause a thickness gradient along the radial direction of the film due to the uneven evaporation rate upon spinning. Therefore, toluene is introduced to lower the volatility of the solvent and achieve a uniform layer and thickness. However, simply processing in volatile solvents will still cause the aerogel network to collapse due to surface tension. Thus, the aerogel is functionalized with TMCS to allow for solvent removal without collapsing the aerogel pores [39, 40]. After solvent evaporation, the aerogel network microstructure is penetrated by hollow voids. The percentage of the aerogel layer made up by voids contributes to the low refractive index of the aerogel. The aerogel cavity layer thickness can be controlled from 40 to 600 nm thick through a combination of dilution, layering, and spin speed (Fig. S2a–b). Through the solution-based process given in the schematic in Fig. 2a, a low-index dielectric can be fabricated with a high degree of control over both refractive index and cavity thickness, which is vital in engineering super-iridescent structural color.

The cross-sectional SEM of fabricated aerogel films in Fig. 2b–d shows increased network density as TEOS concentration is increased, while the void percentage and RI as calculated through spectroscopic ellipsometry is shown to decrease. This is corroborated by the increase in refractive index by ellipsometry with increasing TEOS concentration (Fig. S1). The increasing refractive index is likely due to the denser SiO_2 network from an increased silica precursor concentration. Aerogel RI is controlled by porosity, which in turn is controlled by TEOS concentration [44, 45]. Through structural engineering, we can

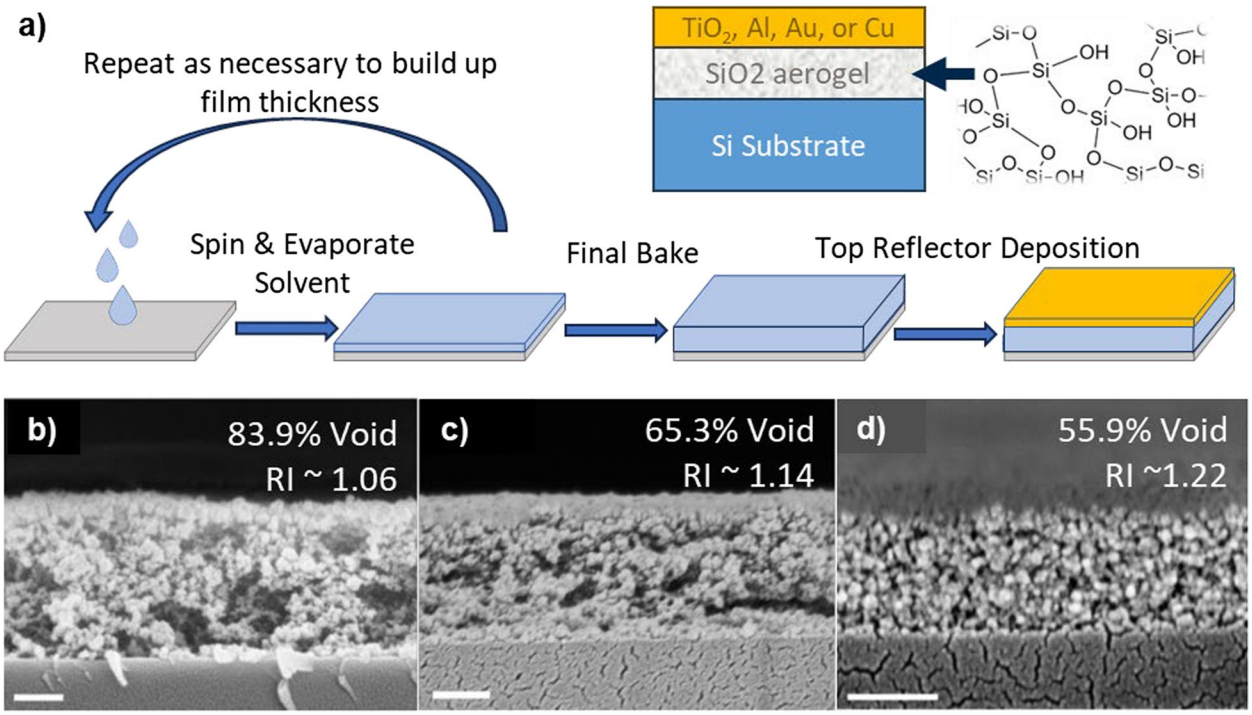

Fig. 2 **a** Schematic of aerogel HLA fabrication. Cross-sectional SEM, refractive index, and percent void of aerogels with refractive index **b** 1.06, **c** 1.14, and **d** 1.22. All scale bars are 200 nm

control the refractive index of the aerogel dielectric and achieve a refractive index as low as 1.06, close to that of air (RI = 1).

Fabrication and characterization of iridescent structural color from aerogel

Due to the high porosity of the aerogel, deposition of the top reflector was done through e-beam deposition or nanoparticle deposition to minimize infiltration of the aerogel by the high RI layer. Two sets of samples were fabricated, with evaporated TiO_2 and Al as the topmost layer, respectively. Both the 38 nm TiO_2/aerogel/Si and 15 nm Al/aerogel/Si structures are capable of a near-complete circle on the CIE diagram between 8 and 65° viewing angles (Fig. 3a) and display distinct colors for the two types of samples. The color of the TiO_2/aerogel/Si HLA transforms from cyan to blue to magenta to yellow at increasing viewing angles, while the color of the Al/aerogel/Si HLA transforms from purple to pink to green to blue (Fig. 3a). The reflection dip minima in the corresponding spectra blue-shifts from 650 to 400 nm (TiO_2) or 540 nm into the UV (Al) with increasing viewing angle from normal (Fig. 3c–d). In either case, the solution-processable aerogel films help to create super-iridescent structural colors.

It should be noted that the particulate nature of the aerogel dispersion can lead to speckling and color non-uniformity. Stronger sonication can be used to further break down aerogel colloids or filtration through a finer mesh can improve the color uniformity of these films.

Figure 4a shows a cross-sectional TEM and elemental analysis of e-beam deposited TiO_2 atop SiO_2 aerogel. The TiO_2 layer follows the contours of the rough aerogel layer and slightly infiltrates into the aerogel due to the porosity

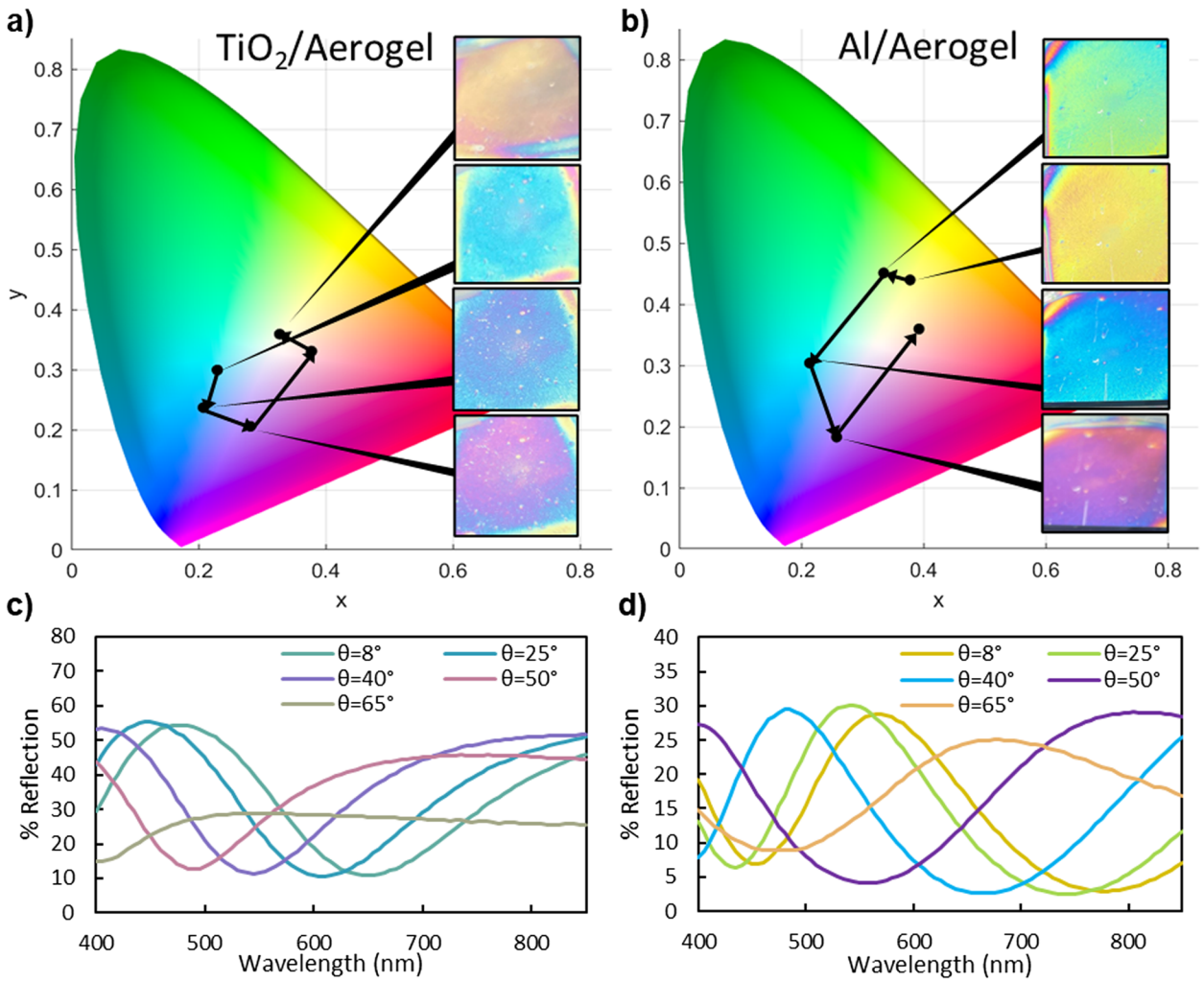

Fig. 3 CIE diagrams and photos of **a** 38 nm TiO_2/aerogel/Si and **b** 15 nm Al/aerogel/Si at viewing angles from 8 to 65°. Photos were captured outdoors in sunlight through a polarizing lens. Angle-resolved reflection spectra of **c** 38 nm TiO_2/aerogel/Si and **d** 15 nm Al/aerogel/Si (right) from 8 to 65°

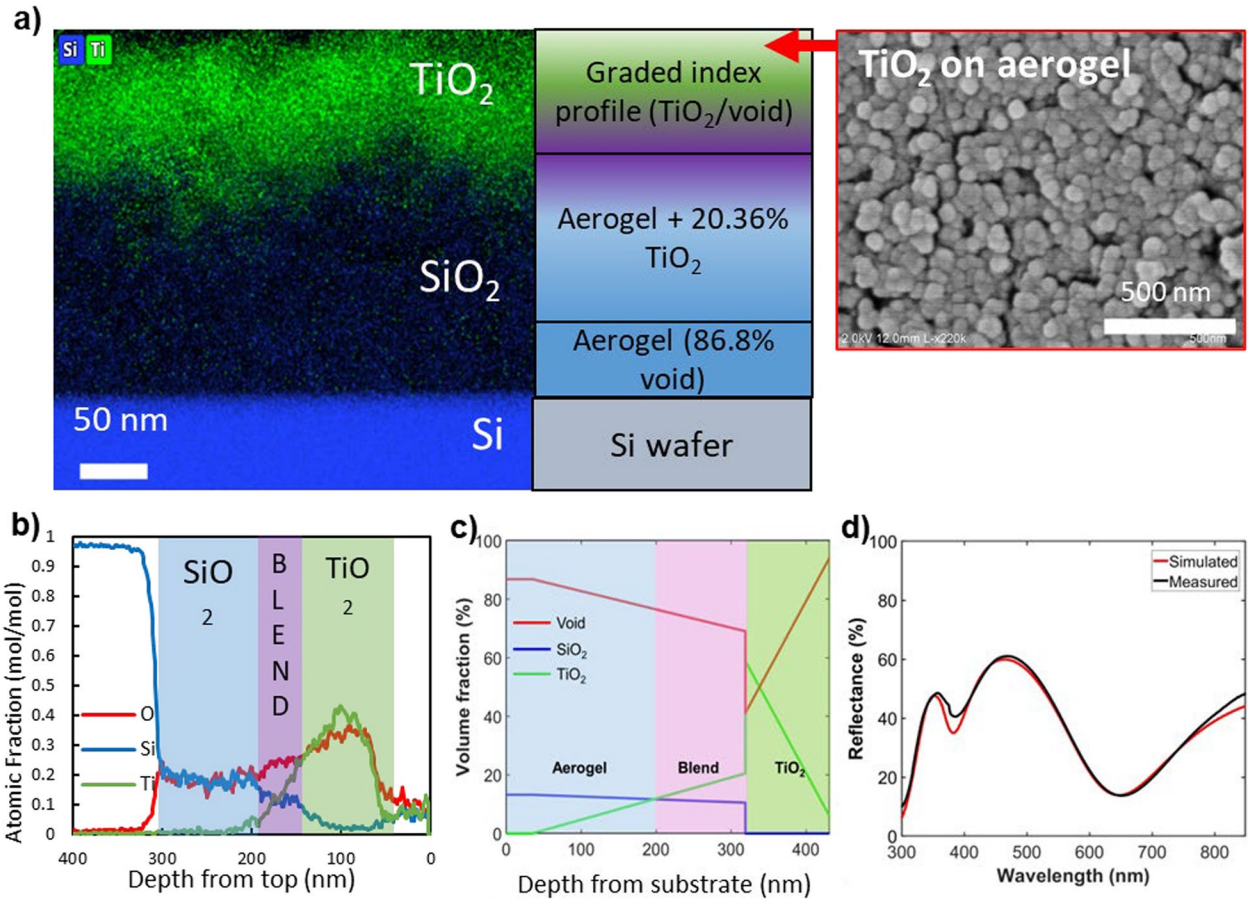

Fig. 4 **a** Elemental mapping of HLA with schematic profile of structure adjusted for blending and surface roughness. **b** Atomic fraction depth profile of O, Si, and Ti in HLA. **c** Volume fraction depth profile of TiO_2, SiO_2, and void calculated from adjusted fitting profile using EMA method. **d** Comparison between measured reflection spectrum and simulated reflection spectrum adjusted for blend and roughness

of the aerogel layer, shown by the blend layer in Fig. 4b. Compared to a pristine TiO_2 film on Si (Fig. S3), TiO_2 follows the surface topology of the aerogel, resulting in a rough film (Fig. 4a). The scattering effect of light becomes pronounced when forming a TiO_2/aerogel/Si multilayer structure due to the roughened interface, with strongest light scattering in the UV range, the reduced scattering with increasing refractive index of the aerogel layer due to reduced porosity and interfacial roughness (Fig. S5b). The film shows a reflection max of about 50% and a minimum of 15% across all angles tested, and an iridescent structural color was successfully fabricated. The blend layer and scattering of the fabricated HLA are responsible for the deviation of the measured reflection spectra from the simulated reflection spectra based on uniform layer thickness and sharp interfaces (Fig. S5a).

To investigate the impact of the blend layer and HLA scattering, we consider TiO_2 penetration, surface roughness, and fill fraction in our simulation model. The updated model is shown in Fig. 4a and accounts for the partial penetration of TiO_2 into the aerogel layer, leading to the mixed layer observed in the elemental depth profile (Fig. 4a and b). This is consistent with the volume fraction depth profile in Fig. 4c calculated through the Effective Medium Approximation (EMA) method, showing that the aerogel and aerogel/TiO_2 blend layers are still highly porous. Our EMA model is calculated by using Transfer Matrix Theory, and we considered that each of layers were partially mixed with SiO_2, TiO_2, and air, with more intermixing at the interface of the layers. To calculate EMA for the mixed layers, we implemented Bruggeman theory, which is used in the context of dielectric materials consisting of a mixture of two or more different materials. In our model, the aerogel layer was treated to be mixed with air and SiO_2, and the top portion of the aerogel layer was divided into several layers that were mixed with different portions of TiO_2 particles. The portion of TiO_2 in the aerogel layers gradually increases from 0 to 20.36%, and the thickness of the bare aerogel layer is 33.2 nm. This represents the fact that the TiO_2 particles

penetrate the partial aerogel layer due to the porosity of the aerogel network.

At the interface between the aerogel and the TiO_2 layer, the porosity reduces to 41.3%, indicating a transition from the aerogel to TiO_2 (Fig. 4c). Due to the high surface roughness of TiO_2 (Fig. 4a), the porosity gradually increases again towards the surface of the film up to 94.1%. With these considerations, the adjusted model fits well to the experimental reflection spectrum (Fig. 4d); thus, the deviations from the ideal case can be attributed to partial TiO_2 penetration into the aerogel and surface roughness.

Aerogel index has strongest effect on reflection dip travel

Iridescence is an optical phenomenon in which hue changes with angle of observation. In the reflection spectrum of a subtractive structural color surface, this manifests as changes to the location of the reflection dip as the resonant wavelength changes. Notably, as viewing angle increases, the resonant wavelength decreases, causing the reflection dip to shift to shorter wavelengths.

We can use Bragg's law to understand the angle-dependent reflection spectrum behavior of a thin film structure (assuming air as the incident medium):

$$N\lambda = 2nd\left[1 - \left(\frac{1}{n}\right)^2 \sin^2\theta_i\right]^{\frac{1}{2}} \quad (1)$$

where λ, n, d, and N are the resonant wavelength, the refractive index of the film, the layer thickness, and an arbitrary integer, respectively (Fig. 1a) [28, 29]. The angle-dependency can then be described as the change of resonance wavelength with respect to the incident angle:

$$\frac{\delta\lambda}{\delta\theta} = A\left[n^4 - n^2\sin^2\theta_i\right]^{-\frac{1}{2}} \quad (2)$$

where:

$$A = -2Nnd\sin\theta_i\cos\theta_i \quad (3)$$

According to Eq. 2, we note the refractive index of the stratified medium plays a very important role in determining the overall angle sensitivity. As shown in Fig. 1b, a very large shift in resonance wavelength is observed with a low medium refractive index, while the resonance wavelength hardly moves when the medium refractive index becomes high. A further investigation on the angle sensitivity $\frac{\delta\lambda}{\delta\theta}$ reveals a higher sensitivity is achieved when the incident angle increases until a large angle of 50–60° is reached (Fig. 1c). In other words, the color change would become more rapid at larger angles for low refractive index medium. To determine the influence aerogel RI on the color travel, reflection spectra were collected between 8 and 65° and the dip minima position was recorded for each angle. The collected reflection spectra from which these curves were determined are found in Figs. S6–S8.

Aerogel refractive index has a significant effect on reflection dip minima shift. Figure 5a plots the reflection dip minima wavelength against the measured viewing angle in degrees. A first-order approximation linear slope is fitted to the plot and compared across different refractive indices. By increasing the refractive index from 1.05 to 1.22, the slope of the minima wavelength vs. angle plot decreases, corroborating the inversely proportional relationship between refractive index and $\frac{\delta\lambda}{\delta\theta}$ in Eq. 3. Changes in $\frac{\delta\lambda}{\delta\theta}$ with refractive index (Fig. 5b) and viewing angle (Fig. 5c) were calculated from the experimental data. The resulting trends match well to the trends of $\frac{\delta\lambda}{\delta\theta}$ vs. refractive index and viewing angle calculated from Eqs. 3 and 4 and show that $\frac{\delta\lambda}{\delta\theta}$ decreases with increasing refractive index and increases with increased viewing angle. This angle-dependent behavior is also observed in the model presented in the "Fabrication and Characterization of Iridescent Structural Color from Aerogel" section with roughness and blending accounted for. Figure 5d shows good agreement between the measured data and simulation, with rapid blue-shifting of resonance wavelength at increased viewing angles. Overall, as the viewing angle is increased from normal, the reflection dip minima travel to shorter wavelengths (blue-shifted), and this effect is strongly dependent on the aerogel refractive index.

Compared to the aerogel refractive index, cavity thickness does not have much of an effect on the slope of the reflection dip minima vs. angle plot seen in Fig. S9a. As thickness is increased, the reflection dip minima shift to longer wavelengths, only to shift to shorter wavelengths at increasing viewing angles from normal. The change is more notable as aerogel thickness is increased to 349 nm. At low film thickness (210 nm), fewer data points were collected due to the shift of the reflection dip into the UV range at 30° from normal. TiO_2 thickness does not have much of an effect on reflection dip minima shift as seen in Fig. S9b. Our results demonstrate that the aerogel refractive index has the strongest effect on reflection dip minima shift and match the theoretical trends.

Applications involving functional adjustments to refractive index

Since the porous space gives rise to an ultra-low refractive index, these pores can also be filled with other mediums, making the structure a colorimetric sensor to the filled medium. Also, the aerogel HLA structure can be expanded upon through the inclusion of plasmonic nanomaterials. In this example, negatively charged gold nanoparticles (AuNPs) were deposited partially into the

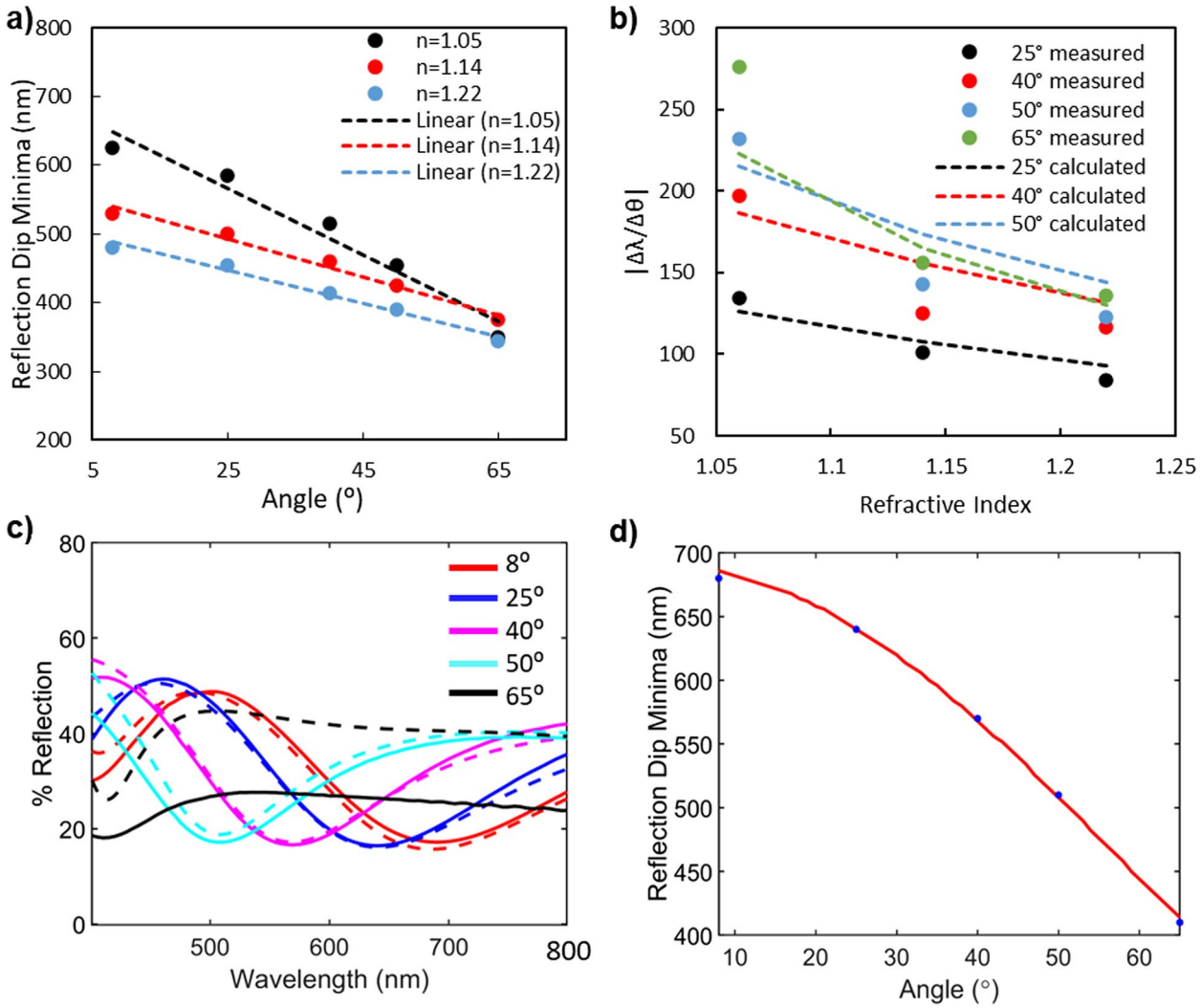

Fig. 5 **a** Reflection dip minima of aerogel HLA from 8 to 65° viewing angles at RI 1.06–1.22. **b** Refractive index effect on $\frac{\delta\lambda}{\delta\theta}$ at viewing angles from 25 to 65° as measured (dots) and calculated from Eqs. 3 and 4 (dotted lines, $N=1$, $d=180$ nm). **c** Agreement between experimental (solid lines) and simulated (dashed lines) angle-resolved reflection spectra of RI 1.06 aerogel HLA. **d** Agreement between experimental and simulated angle travel of RI 1.06 aerogel HLA

aerogel after functionalization with positively charged groups through ionic interactions. The resulting films and their reflection performance can be seen in Fig. 6a–b. Deposition of AuNPs does not negatively affect the color travel, but expands the range of achievable colors towards purple, orange, and yellow as seen in Fig. 6a. AuNPs also impart absorption around 500–530 nm, which can be seen as a dip in the reflection spectrum whose location remains constant even with changes to the viewing angle as seen in Fig. 6b [46, 47]. As the dip caused by cavity resonance blue-shifts with increased viewing angle, the dip caused by AuNP absorption remains relatively in place, leading to multiple dips observed in the reflection spectrum at high viewing angles and thus generation of unique colors such as orange at certain angles as seen in Fig. 6b. Thus, the shape of the reflection spectrum and therefore the observed color can be tuned by adding absorbing nanomaterials, thereby expanding the range of achievable colors without sacrificing iridescence.

Replacing the pores with other mediums can also impart sensing abilities through changes in refractive index. We therefore carefully cast a drop of solvent onto the 15-nm Al/SiO2 aerogel/Si film where the solvent gets quickly absorbed into the porous structure followed by a quick color change. As shown in Fig. 6c, a higher-order reflection peak shows up once the film gets soaked in ethanol. This can be understood as a surge in average refractive index once the air voids are

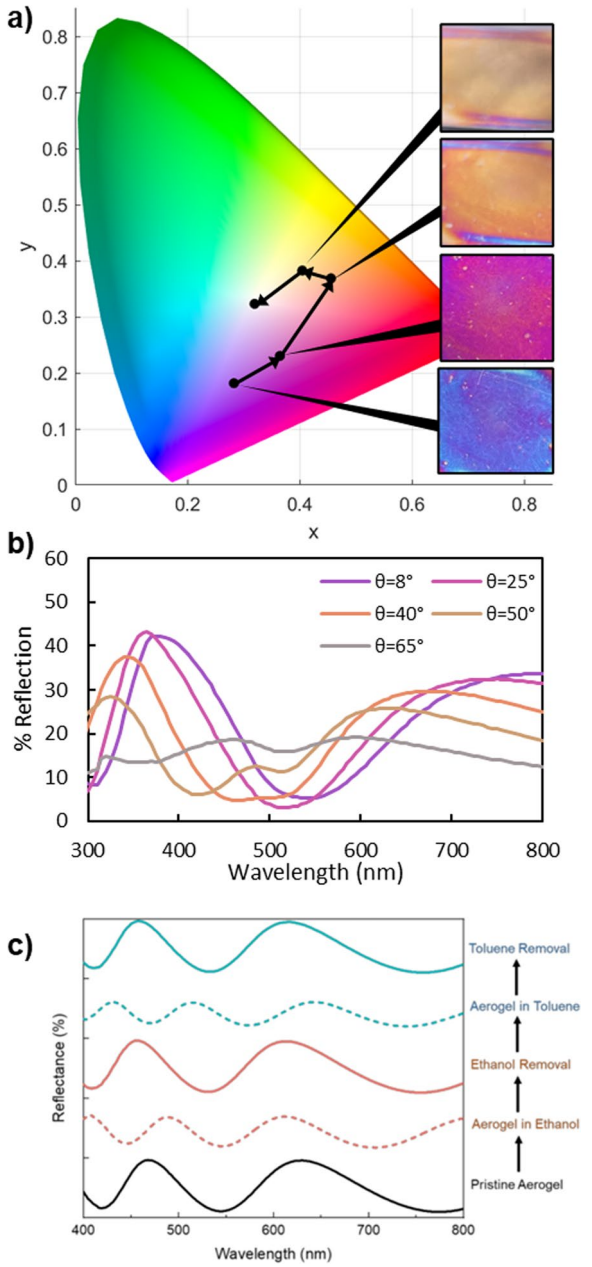

Fig. 6 **a** CIE diagram and photos of 25 nm TiO2/340 nm AuNP-aerogel/Si at viewing angles from 8 to 65°. Photos were captured outdoors in sunlight. **b** Angle-resolved reflection spectra of 25 nm TiO2/340 nm AuNP-aerogel/Si from 8 to 65°. **c** Reflection spectra of 15 nm Al/aerogel (RI = 1.07)/Si immersed in solvents (i.e., ethanol and toluene) and upon solvent removal

replaced with ethanol (RI = 1.36) while maintaining the overall thickness of the film, which leads to a larger optical path length and therefore a higher-order resonance. Once the ethanol gets evaporated, the reflection spectrum recovers to its pristine value, indicating the porous structure has not been destructed. Similar behavior is observed with toluene (RI = 1.50) but with a red shift in the higher order resonance as the higher refractive index of toluene gives an even longer optical path. Again, the reflection spectrum recovers to the original pristine film upon toluene removal. We can then expect such porous aerogel based could potentially serve as a colorimetric index sensor with further device engineering taken into play [48, 49].

Conclusion

In summary, we have successfully fabricated and characterized iridescent structural color using an ultra-low-index aerogel dielectric as a cavity and high-index TiO_2 as a top reflector in an HLA cavity. We have demonstrated control over reflected color, reflection spectrum, and color travel through changes in aerogel thickness and refractive index. We have expanded the possibilities of this porous aerogel network by demonstrating its potential for functionalization by plasmonic nanomaterials through a simple solution process and its potential for use as a chromatic index sensor. Further work will move towards complete solution fabrication of aerogel-incorporated materials for use in pigments on a larger scale. The ultra-low index aerogel can impart new possibilities otherwise unattainable in other optical elements, and hope this can inspire other researchers to explore these functionalities.

Supplementary Information

The online version contains supplementary material available at https://doi.org/10.1007/s44374-024-00001-2.

Supplementary Material 1. Additional experimental details, materials, methods, and data, including angle-resolved reflection spectra and corresponding CIE color travel diagrams. Table S1 – Synthesis quantities for producing aerogel films of RI = 1.06–1.22. Figure S1 – Refractive index of aerogels across visible light range. Figure S2 – Range of achievable thicknesses of aerogel films through spin speed, dilution, and layering. Figure S3 – Smooth TiO2 on Si wafer. Figure S4 – TEM elemental mapping. Figure S5 – Impact of Morphological Non-idealities of fabricated aerogel HLA on Simulated and Experimental Reflection Spectrum of HLA. Figure S6 – Angle resolved spectra by Cavity Refractive Index and corresponding CIE Color Travel Diagrams. Figure S7 – Angle resolved spectra by Cavity thickness and corresponding CIE Color Travel Diagrams. Figure S8 – Angle resolved spectra by TiO2 thickness and corresponding CIE Color Travel Diagrams. Figure S9 – Angle dependency on cavity and TiO2 thickness and corresponding CIE Color Travel Diagrams. Figure S10 – Changes in angle-dependent behavior by light polarization.

Acknowledgements

J.J.P. would like to acknowledge Dr. Kai Sun for TEM/EDS imaging; Prof. Neil Dasgupta, Prof. Andrej Lenert, Dr. Julia Lenef, and Dr. Ying Qi for characterization technique assistance; Dr. Jianing Sun and Dr. Nina Hong for ellipsometry fitting model development assistance; Tarana Kaovasia for TMM code development assistance; Dr. Wei-Kuan Lin, Dr. Aagnik Pant, Mohammad Ali, Amanda Wang, and Tarana Kaovasia for many helpful discussions. W. J. F. thanks Prof. Joseph J. Talghader for many helpful discussions. S.W.C thanks the Michigan Center for Materials Characterization, and the Lurie Nanofabrication Facility for use of the instruments and staff assistance.

Authors' contributions
L.J.G conceived and directed the project. W.F. developed the aerogel synthesis process. J.P., W. F. and S. W. C carried out the experiment and characterizations. H. K simulated the optical responses by analyzing and modeling the structure with diffused interfaces. J.P and W. F. wrote the manuscript, and L.J.G edited it. All authors provided input to the figures and reviewed the manuscript.

Data availability
Data is provided within the manuscript or supplementary information file.

Declarations

Competing interests
The content of the manuscript is the subject of a US provisional patent application.

Received: 29 August 2024 Accepted: 7 November 2024
Published online: 12 December 2024

References

1. Wang D, Liu Z, Wang H, Li M, Guo LJ, Zhang C (2023) Structural color generation: From layered thin films to optical metasurfaces. Nanophotonics 12(6):1019–1081. https://doi.org/10.1515/nanoph-2022-0063
2. Meadows MG, Butler MW, Morehouse NI, Taylor LA, Toomey MB, McGraw KJ, Rutowski RL (2009) Iridescence: views from many angles. J R Soc Interface 6(2):S107–S113. https://doi.org/10.1098/rsif.2009.0013.focus
3. ElKabbash M, Hoffman N, Lininger AR, Jalil SA, Letsou T, Hinczewski M, Strangi G, Guo C (2023) Fano resonant optical coatings platform for full gamut and high purity structural colors. Nat Commun 14:3960. https://doi.org/10.1038/s41467-023-39602-2
4. Tabata M, Adachi I, Ishii Y, Kawai H, Sumiyoshi T, Yokogawa H (2010) Development of transparent silica aerogel over a wide range of densities. Nucl Instrum Methods Phys Res 623(1):339–341. https://doi.org/10.1016/j.nima.2010.02.241
5. Heo DD, Oh YJ, Jun BS (2007) Nano structured silica aerogel films by dip-coating process. Solid State Phenomen 124–126:1221–1224. https://doi.org/10.4028/www.scientific.net/SSP.124-126.1221
6. Yang HS, Choi SY, Hyun SH, Park HH, Hong JK (1997) Ambient-dried low dielectric SiO_2 aerogel thin film. J Non-cryst Solids 221(2–3):151–156. https://doi.org/10.1016/S0022-3093(97)00335-9
7. Kim Y, Baek S, Gupta P, Kim C, Chang K, Ryu SP, Kang H, Kim WS, Myoung J, Park W, Kim K (2019) Air-like plasmonics with ultralow-refractive-index silica aerogels. Sci. Rep. 9:2265. https://doi.org/10.1038/s41598-019-38859-2
8. Thundathil MA, Lai W, Noailles L, Dunn BS, Haile SM (2004) High surface-area ceria aerogel. J Am Ceram Soc 87(8):1442–1445. https://doi.org/10.1111/j.1551-2916.2004.01442.x
9. Yang H, Zhu W, Sun S, Guo X (2014) Preparation of monolithic titania aerogels with high surface area by a sol-gel process combined surface modification. RSC Adv 4(62):32934–32940. https://doi.org/10.1039/C4RA03812F
10. Peng F, Jiang Y, Feng J, Li L, Cai H, Feng J (2020) A facile method to fabricate monolithic alumina–silica aerogels with high surface areas and good mechanical properties. J Eur Ceram Soc 40(6):2480–2488. https://doi.org/10.1016/j.jeurceramsoc.2020.01.058
11. Cheng Y, Zhou S, Hu P, Zhao G, Li Y, Zhang X, Han W (2017) Enhanced mechanical, thermal, and electric properties of graphene aerogels via supercritical ethanol drying and high-temperature thermal reduction. Sci Rep 7:1439. https://doi.org/10.1038/s41598-017-01601-x
12. Wang X, Xie P, Wan K, Miao Y, Liu Z, Li X, Wang C (2021) Mechanically strong, low thermal conductivity and improved thermal stability polyvinyl alcohol–graphene–nanocellulose aerogel. Gels 7(4):170. https://doi.org/10.3390/gels7040170
13. Ni XY, Wang J, Liu GW, Zhang ZH, Shen J, Zhou B, Wu GM (2012) Preparation and properties of super insulation material SiO2 Aerogel. Adv Mat Res 516–517:1531–1535. https://doi.org/10.4028/www.scientific.net/AMR.516-517.1531
14. Wang J, Liu D, Li Q, Chen C, Chen Z, Song P, Hao J, Li Y, Fakhrhoseini S, Naebe M, Wang X, Lei W (2019) Lightweight, superelastic yet thermoconductive boron nitride nanocomposite aerogel for thermal energy regulation. ACS Nano 13(7):7860–7870. https://doi.org/10.1021/acsnano.9b02182
15. Zhang Y, Li J, Liu H, Li Y, Rui J, Da H, Chen Z (2020) Microencapsulated phase change materials composited Al_2O_3–SiO_2 aerogel and the thermal regulation properties. J Sol-gel Sci Techn 96:627–635. https://doi.org/10.1007/s10971-020-05363-3
16. Thomas B, Geng S, Sain M, Oksman K (2021) Hetero-porous, high-surface area green carbon aerogels for the next-generation energy storage applications. Nanomaterials 11(3):653. https://doi.org/10.3390/nano11030653
17. Lin P, Xie J, He Y, Lu X, Li W, Fang J, Yan S, Zhang L, Sheng X, Chen Y (2020) MXene aerogel-based phase change materials toward solar energy conversion. Sol Energ Mat Sol C 206:110229. https://doi.org/10.1016/j.solmat.2019.110229
18. Liu H, Du H, Zheng T, Liu K, Ji X, Xu T, Zhang X, Si C (2021) Cellulose based composite foams and aerogels for advanced energy storage devices. Chem Eng J 426:130817. https://doi.org/10.1016/j.cej.2021.130817
19. Rey G, Vivod S, Singla S, Benyo T, King J, Chuang SSC, Dhinojwala A (2021) Improved polydopamine deposition in amine-functionalized silica aerogels for enhanced UV absorption. ACS Appl Mater Interfaces 13(34):41084–41093. https://doi.org/10.1021/acsami.1c10879
20. Grogan MDW, Heck SC, Hood KM, Maier SA, Birks TA (2011) Structure of plasmonic aerogel and the breakdown of the effective medium approximation. Opt Lett 36(3):358–360. https://doi.org/10.1364/OL.36.000358
21. Hotaling SP (1993) Ultra-low density aerogel optical applications. J Mater Res 8:352–355. https://doi.org/10.1557/JMR.1993.0352
22. Kim C, Baek S, Ryu Y, Kim Y, Shin D, Lee CW, Park W, Urbas AM, Kang G, Kim K (2018) Large-scale nanoporous metal-coated silica aerogels for high SERS effect improvement. Sci Rep 8:15144. https://doi.org/10.1038/s41598-018-33539-z
23. Ellebracht NC, Jones CW (2019) Functionalized cellulose nanofibril aerogels as cooperative acid-base organocatalysts for liquid flow reactions. Carbohyd Polym 233:115825. https://doi.org/10.1016/j.carbpol.2019.115825
24. Leung CK, Lu L, Liu Y, Cheng HS, Tse JH (2020) Optical and thermal performance analysis of aerogel glazing technology in a commercial building of Hong Kong. Energy Built Environ 1(2):215–233. https://doi.org/10.1016/j.enbenv.2020.02.001
25. Illera D, Mesa J, Gomez H, Maury H (2018) Cellulose aerogels for thermal insulation in buildings: trends and challenges. Coatings 8(10):345. https://doi.org/10.3390/coatings8100345
26. Wang J, Petit D, Ren S (2020) Transparent thermal insulation silica aerogels. Nanoscale Adv 2(12):5504–5515. https://doi.org/10.1039/D0NA00655F
27. Naeem J, Mazari AA, Akçagün E, Kus Z (2018) Silicaoxide aerogels and its application in firefighter protective clothing. Ind Textila 69(1):50–54. https://doi.org/10.35530/IT.069.01.1399
28. Born M, Wolf E (1999) Principles of optics: electromagnetic theory of propagation, interference, and diffraction of light. Cambridge University Press, London
29. Yang Q, Zhao LR (2008) Characterization of nano-layered multilayer coatings using modified Bragg law. Mater Charact 59(9):1285–1291. https://doi.org/10.1016/j.matchar.2007.11.001
30. Feng WJ, Cheng Y, Guo LJ (2023) Temporal coupled mode analysis of chromaticity in trilayer subtractive structural colors. ACS Photonics 10(8):2784–2792. https://doi.org/10.1021/acsphotonics.3c00481
31. Lee KT, Seo S-Y, Lee JY, Guo LJ (2014) Ultrathin metal-semiconductor-metal resonator for angle invariant visible band transmission filters. Appl Phys Lett 104(23):231112. https://doi.org/10.1063/1.4883494
32. Ji CG, Lee KT, Xu T, Zhou J, Park HJ, Guo LJ (2017) Engineering light at the nanoscale: structural color filters and broadband perfect absorbers. Adv Optical Mater 5(20):1700368. https://doi.org/10.1002/adom.201700368
33. Mayer T, Yamanaka SA, Zieba J (2000) Color-shifting pigments and foils with luminescent coatings. US 6565 770 B1
34. Zimmermann L, Weibel M, Caseri W, Suter UW, Walther P (1992) Polymer nanocomposites with "ultralow" refractive index. Polym Adv Technol 4(1):1–7. https://doi.org/10.1002/pat.1993.220040101
35. Chi F, Yan L, Yan H, Jiang B, Lv H, Yuan X (2012) Ultralow-refractive-index optical thin films through nanoscale etching of ordered mesoporous

silica films. Opt Lett 37(9):1406–1408. https://doi.org/10.1364/OL.37.001406
36. Chi F, Yan L, Lv H, Yan H, Yuan X, Jiang B (2012) Sol-gel preparation of ultralow refractive index magnesium fluoride optical films for broadband antireflective coatings. Nanosci Nanotech 4(4):441–444. https://doi.org/10.1166/nnl.2012.1330
37. Yamaguchi M, Nakayama H, Yamada K, Imai H (2009) Ultralow refractive index coatings consisting of mesoporous silica nanoparticles. Opt Lett 34(13):2060–2062. https://doi.org/10.1364/ol.34.002060
38. Hierro-Rodriguez A, Rocha-Rodigues P, Valdés-Bango F, Alameda JM, Jorge PAS, Santos JL, Araujo JP, Teixeira JM, Guerreiro A (2015) On the anodic aluminum oxide refractive index of nanoporous templates. J Phys D Appl Phys 48(45):455105. https://doi.org/10.1088/0022-3727/48/45/455105
39. Lin P, Mah M, Randi J, DeFrances S, Bernot D, Talghader JJ (2023) High average power optical properties of silica aerogel thin film. Thin Solid Films 768:139722. https://doi.org/10.1016/j.tsf.2023.139722
40. Lin P, Mah M, Talghader JJ (2022) Synthesis and characterizations of a very low index silica aerogel optical thin film. In: Optical Interference Coatings Conference (OIC) Technical Digest Series, Whistler, British Columbia, Canada, Paper WD.5
41. Brinker CJ, Scherer GW (1990) Sol-gel science: the physics and chemistry of sol-gel processing. Academic Press, Boston
42. Pettersson LAA, Roman LS, Inganäs O (1999) Modeling photocurrent action spectra of photovoltaic devices based on organic thin films. J Appl Phys 86(1):487–496. https://doi.org/10.1063/1.370757
43. Prakash SS, Brinker CJ, Hurd A, Rao SM (1995) Silica aerogel films prepared at ambient pressure by using surface derivatization to induce reversible drying shrinkage. Nature 374:439–443. https://doi.org/10.1038/374439a0
44. Feng WJ, Ji C, Guo LJ (2023) Primary and secondary reflective color realized by full-solution-processed multi-layer structures. Adv Opt Mater 11(15):2300456. https://doi.org/10.1002/adom.202300456
45. Tajima N, Murotani H, Matsudaira T (2023) Optical multicoating using low-refractive-index SiO_2 optical thin films deposited by sputtering and electron beam evaporation. Thin Solid Films 776:139824. https://doi.org/10.1016/j.tsf.2023.139824
46. He YQ, Liu SP, Kong L, Liu ZF (2005) A study on the sizes and concentrations of gold nanoparticles by spectra of absorption, resonance Rayleigh scattering and resonance non-linear scattering. Spectrochim Acta A Mol Biomol Spectrosc 61(13–14):2861–2866. https://doi.org/10.1016/j.saa.2004.10.035
47. Haiss W, Thanh NTK, Aveyard J, Fernig DG (2007) Determination of Size and Concentration of Gold Nanoparticles from UV–Vis Spectra. Anal Chem 79(11):4215–4221. https://doi.org/10.1021/ac0702084
48. Ivanov II, Klyui NI, Skryshevsky VA (2019) Colorimetric analysis of optical reflection from thin porous silicon for detection of organic liquids. Sensors Actuators B Chem 280:102–108. https://doi.org/10.1016/j.snb.2018.10.021
49. Talukdar TH, McCoy B, Timmins SK, Rykman JD (2020) Hyperchromatic structural color for perceptually enhanced sensing by the naked eye. Proc National Acad Sci 117(48):30107–30117. https://doi.org/10.1073/pnas.2009162117

Publisher's Note